Identified-particle production in Xe + Xe collisions at $\sqrt{s_{NN}} = 5.44$ TeV using a multiphase transport model

Rutuparna Rath, Sushanta Tripathy, Raghunath Sahoo,* and Sudipan De†
Discipline of Physics, School of Basic Sciences, Indian Institute of Technology Indore, Simrol, Indore 453552, India

Mohammed Younus
Department of Physics, Nelson Mandela University, Port Elizabeth 6031, South Africa

(Received 15 January 2019; published 17 June 2019)

Xe+Xe collisions at relativistic energies provide us with an opportunity to study a possible system with deconfined quarks and gluons, whose size is in between those produced by $p + p$ and Pb+Pb collisions. In the present work, we have used a multiphase transport (AMPT) model with nuclear deformation to study the identified particle production, such as $(\pi^+ + \pi^-)$, $(K^+ + K^-)$, K^0_s, $(p + \bar{p})$, ϕ, and $(\Lambda + \bar{\Lambda})$ in Xe+Xe collisions at $\sqrt{s_{NN}} = 5.44$ TeV. We study the p_T spectra, integrated yield, and p_T-differential and p_T-integrated particle ratios to $(\pi^+ + \pi^-)$ and $(K^+ + K^-)$ as a function of collision centrality. The particle ratios are focused on strange to nonstrange ratios and baryon to meson ratios. The effect of deformations has also been highlighted by comparing our results to the nondeformation case. We have also compared the results from AMPT string melting and the AMPT default version to explore possible effects of the coalescence mechanism. We observe that the differential particle ratios show strong dependence on centrality while the integrated particle ratios show no centrality dependence. We give a thermal model estimation of chemical freeze-out temperature and the Boltzmann-Gibbs Blast Wave analysis of kinetic freeze-out temperature and collective radial flow in Xe+Xe collisions at $\sqrt{s_{NN}} = 5.44$ TeV.

DOI: 10.1103/PhysRevC.99.064903

I. INTRODUCTION

Ultrarelativistic heavy ion collision experiments conducted at the BNL Relativistic Heavy Ion Collider (RHIC) and the CERN Large Hadron Collider (LHC) give us opportunities to peek into the past when the universe was a few microseconds old. The collisions result in a system of deconfined quarks and gluons at very high temperature and density, or quark-gluon plasma (QGP) [1]. Till recent times, mainly symmetrical nuclei such as lead (Pb) ions or assumed spherical gold (Au) ions have been used to collide and form QGP. Recently, interest has grown in conducting experiments with intrinsically deformed nuclei. Experiments have been conducted at RHIC with uranium (U), which is heavier than gold and lead ions and is considered to be highly deformed (lead ions have zero deformity). A comparison of central collisions of spherical nuclei with those of deformed nuclei helps in establishing if the elliptic flow observed in heavy-ion collisions, which is considered as a signature of QGP, is an initial state effect [2–4]. In the case of a deformed nuclei collision, one expects the charged particle multiplicity density in the transverse phase space to be higher as compared to the collision of spherical nuclei [5–7]. Particle density per unit volume in ideal hydrodynamical models is independent of mass number of the colliding species. A violation of scaling behavior is seen in the observables due to the deformed structures of the colliding nuclei [8].

The LHC has collided xenon (^{129}Xe) ions at $\sqrt{s_{NN}} = 5.44$ TeV to bridge the final state multiplicity gap between the larger Pb-ion systems and smaller systems like $p + p$ and $p +$ Pb. The new findings at the LHC show that the identified particle production as a function of normalized charged particle multiplicity is independent of collision species and collision energy [9]. Eventually, the final state multiplicity density of the system drives the dynamics of particle production. In view of this, Xe+Xe collisions serves to bridge the multiplicity gap among $p + p$, p+Pb, and Pb+Pb collisions and to help in the observation of a universal scaling. It is also observed at the LHC that the Xe+Xe collision system violates the quark participant scaling of charged particle production, similar to other collision species with spherical nuclei [10–15]. In addition, Xe being a deformed nucleus would help in understanding many new features like those observed at the RHIC using U+U collisions, but at a much higher collision energy. It has been shown recently that intrinsic deformities may affect particle flows for central collisions while for peripheral collisions this effect is negligible [16].

*Corresponding author: raghunath.sahoo@cern.ch
†Presently at NISER, Bhubaneswar.

Let us now briefly discuss the particle production in relativistic heavy ion collisions. Heavy ion collisions produce a system of deconfined quarks and gluons for infinitesimally small time, and soon disintegrate by forming hadrons. While initially we have only nucleons and their up and down quarks within the nuclei interacting during collisions, almost all types of known hadrons (including nucleons) are finally detected, and this indicates that all six types of quarks and many more gluons are produced (also photons, leptons) which were absent initially. Study of such enhancement in particle density in comparison to initial ground state nuclear density gives us the direct proof of the high-temperature and dense state of quarks and gluons called QGP. Particle ratios, mainly ratios of different hadrons, give us a direct picture of such enhancement of different quarks and also how they behave and interact as part of the bulk medium [17]. In particular, it is believed that medium flow [18–20] from the point of the collision as well as any form of fluctuation or anisotropy in the initial stages of collision may greatly determine the spectral shape and nature of these ratios. In this context, one may be tempted to note that the momentum anisotropies which are the results of nuclei colliding at different impact parameters may affect the particle ratios. This particular aspect is currently being investigated in many experimental and theoretical studies. As mentioned earlier in the Introduction, till recent times, we have used either Au or Pb nuclei, which have either assumed spherical shape or zero deformities, to investigate the issues. However, it has become desirable to explore the effect of nuclear deformation on particle production and its effect on properties of matter which are sensitive to nuclear geometry. In this paper we introduce nonzero deformities to the Xe nuclei to study effects on the particle production. Collisions of xenon nuclei should provide us with a much cleaner system than Pb nuclei as well as a more dense and hot QGP medium than proton collisions, $p+p$, might form at comparable collision energies. In addition to this, we have effects due to deformations which we may be able to discern with much less effort than in the case of U+U collisions.

In this paper we have included deformation to the nucleus defined within AMPT model. We will discuss this briefly in one of the following sections. We have calculated particle ratios for the charged hadrons and have tried to find out the effects of the deformation on particle production. The paper is organized as follows. The present introductory section is followed by sections on formalism and results and discussions. These are followed by conclusion at the end.

II. FORMALISM

A multiphase transport (AMPT) model

AMPT is a hybrid transport model which contains four components, namely, initialization of collisions, parton transport after initialization, hadronization mechanism, and hadron transport [21]. The initialization of the model follows HIJING model [22] and calculates the differential cross section of the produced minijet particles in $p+p$ collisions, which is given by

$$\frac{d\sigma}{dp_T^2\,dy_1\,dy_2} = K\sum_{a,b} x_1 f_a\left(x_1, p_{T1}^2\right) x_2 f_2\left(x_2, p_{T2}^2\right)\frac{d\hat{\sigma}_{ab}}{d\hat{t}}, \quad (1)$$

where σ is the produced particles cross section and $\hat{t}$ is the momentum transfer during partonic interactions in $p+p$ collisions. x_i's are the momentum fraction of the mother protons which are carried by interacting partons and $f(x, p_T^2)$'s are the parton density functions (PDFs). The produced partons calculated in $p+p$ collisions are then converted into $p+A$ and $A+A$ collisions by incorporating a parametrized shadowing function and nuclear overlap function using the in-built Glauber model within HIJING. In the case of the Pb nucleus, we use the Woods-Saxon (WS) [23] distribution to define the distribution of nucleons (HIJING). For a deformed nucleus such as xenon, we may include the deformation parameter β_n along with spherical harmonics $Y_{nl}(\theta)$ in the WS function [6,24–27]. This is known as the modified Woods-Saxon (MWS) density distribution. We have used MWS within the HIJING model to calculate initial distributions of partons etc., for tip, body, or random configuration collisions of xenon nuclei. Let us now describe briefly MWS. Nucleon density in HIJING is usually written as a three parameter Fermi distribution [28]:

$$\rho(r) = \rho_0\left[\frac{1+w(r/R)^2}{1+\exp[(r-R)/a]}\right]. \quad (2)$$

Here ρ_0 is the nuclear matter density in the center of the nucleus, R is the radius of the nucleus from its center. The parameter a is the skin depth or surface thickness, r is a position parameter and distance of any point from the center of the nucleus, and w is the deviation from a smooth spherical surface. A Au^{197} or Pb^{208} nucleus is assumed here to have uniform distribution of nucleons in its approximately spherical volume and a smooth surface, so that w can be taken to be zero. This reduces Eq. (2) to a Woods-Saxon [29] distribution, which has been used in HIJING in most cases. This may be written as

$$\rho(r) = \frac{\rho_0}{1+\exp[(r-R)/a]}. \quad (3)$$

When we use an axially symmetric or prolate deformed nucleus (viz., U^{238}, Xe^{56}, etc.), nuclear radius R, has been modified to include spherical harmonics. The modified Woods-Saxon nuclear radius [30] may be written as

$$R_{A\Theta} = R[1+\beta_2 Y_{20}(\theta)+\beta_4 Y_{40}(\theta)], \quad (4)$$

where the symbols β_i are deformation parameters. In the case of the xenon nucleus, we have used deformation parameters $\beta_2 = 0.162$ and $\beta_4 = -0.003$ from Ref. [31]. The spherical harmonics Y_{20} and Y_{40} are given by [32]

$$Y_{20}(\theta) = \frac{1}{4}\sqrt{\frac{5}{\pi}}(3\cos^2\theta - 1),$$
$$Y_{40}(\theta) = \frac{3}{16\sqrt{\pi}}(35\cos^4\theta - 30\cos^2\theta + 3). \quad (5)$$

The positions of nucleons within the distribution, $\rho(r)$, are sampled using the volume element $r^2\sin\theta\,dr\,d\theta\,d\phi$ [33,34].

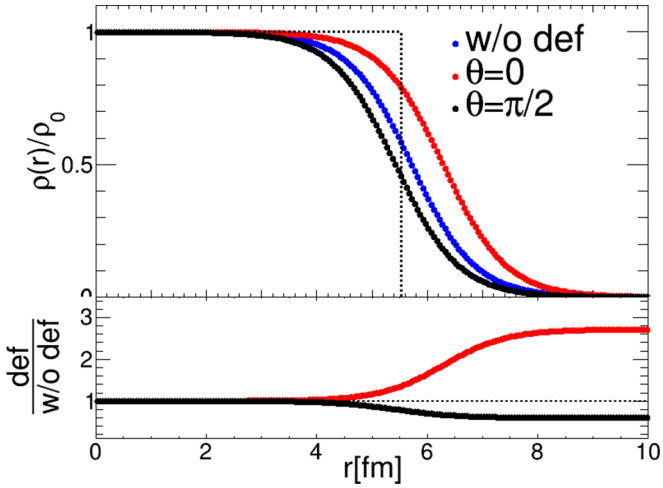

FIG. 1. The nuclear density profile for the xenon nucleus. Shown are the hard sphere, Woods-Saxon, and deformed Woods-Saxon density profiles. The bottom panel shows the ratio of nuclear deformation to nondeformation for the xenon nucleus.

For random orientation of nuclei, position configurations are sampled with both polar angle (angle between major axis and beam axis) Θ in $[0, \pi]$ and azimuthal angle (angle between major axis and impact parameter) Φ within limits $[0, 2\pi]$. Both target and projectile nuclei are rotated event by event in azimuth and polar space. In this paper, calculations have been done only with random orientation, which means unpolarized and averaged value over random Θ and Φ [35]. In Fig. 1, we show the normalized nuclear density profile of xenon with and without deformations. The lower panel shows the ratio of the density profile with nuclear deformation to the case of no deformation.[1]

The initial low-momentum partons, which are separated from high momenta partons by a momentum cutoff of $p_{\mathrm{T}} = 2.0\ \mathrm{GeV}/c$, are produced from parametrized colored string fragmentation mechanisms. The high-p_{T} particles (usually minijets) are sensitive to this momentum cutoff [36]. The produced particles are then initiated into the parton transport part, ZPC (Zhang's parton cascade model) [37], which transports the quarks and gluons using the Boltzmann transport equation, which is given by

$$p^{\mu}\partial_{\mu} f(x, p, t) = C[f]. \tag{6}$$

The leading-order equation showing interactions among partons is approximately given by

$$\frac{d\hat{\sigma}_{gg}}{d\hat{t}} \approx \frac{9\pi\alpha_s^2}{2(\hat{t} - \mu^2)^2}. \tag{7}$$

Here σ_{gg} is the gluon scattering cross section, α_s is the strong coupling constant used in the above equation, and μ^2 is the cutoff used to avoid infrared divergences which can occur if the momentum transfer, $\hat{t}$, goes to zero during scattering. In the string melting version of AMPT (AMPT-SM), meltings of colored strings into low momentum partons also take place at the start of the ZPC, and are calculated using the Lund FRITIOF model of HIJING. This melting phenomenon depends upon spin and flavor of the excited strings. The resulting partons undergo multiple scatterings, which take place when any two partons are within the distance of minimum approach, which is given by $d \leqslant \sqrt{\sigma/\pi}$, where σ is the scattering cross section of the partons. In AMPT-SM, the transported partons are finally hadronized using the coalescence mechanism [38], when two (or three) quarks sharing a close phase space combine to form a meson (or a baryon). The coalescence in AMPT can be shown by the following equation (for, e.g., a meson):

$$\frac{d^3N}{d^3p_M} = g_M \int d^3x_1 d^3x_2 d^3p_1 d^3p_2\, f_q(\vec{x}_1, \vec{p}_1) f_{\bar{q}}(\vec{x}_2, \vec{p}_2) \times \delta^3(\vec{p}_M - \vec{p}_1 - \vec{p}_2)\, f_M(\vec{x}_1 - \vec{x}_2, \vec{p}_1 - \vec{p}_2). \tag{8}$$

Here g_M is the meson degeneracy factor, f_q's are the quark distributions after the evolution, and f_M is the coalescing function commonly called the Wigner function [38]. The produced hadrons undergo further evolution in A Relativistic Transport (ART) mechanism [39,40] via meson-meson, meson-baryon, and baryon-baryon interactions, before final spectra can be observed. The default version of AMPT is known as AMPT-Default, where, instead of coalescing the partons, we have a fragmentation mechanism using Lund fragmentation parameters a and b used for hadronizing the transported partons. However, it can be shown that particle flow and spectra at the mid-p_{T} regions are well explained by the quark coalescence mechanism for hadronization [41–43]. We have used AMPT-SM mode for our calculations. We will return to the discussion of our choice in the results and discussion section. We have used the AMPT version 2.26t7 (released 28 October 2016) in our current work. It is worthwhile to mention that earlier studies of particle elliptic flow in Pb+Pb collisions with AMPT showed greater match with experimental data when large partonic scattering cross section ($\sigma_{gg} \approx 10$ mb) was taken [44,45]. As expected, results with $\sigma_{gg} \approx 10$ mb show greater v_2 than 3 mb. Taking rapidity η as the variable, the difference in 10 and 3 mb results can be seen as a constant multiplication factor, particularly in the central rapidity region [45]. In the present work, we have fixed $\sigma_{gg} = 10$ mb as the cross section for our calculations and the estimation of identified particle ratios. The Lund string fragmentation parameters a and b are kept fixed at their default values of 2.2 and $0.5/\mathrm{GeV}^2$, respectively. It should be noted here that, as we intend to study ϕ and K_s^0 in the final state, we have kept the hadron level decay flagged as "off" for ϕ and K_s^0 throughout our analysis. As expected, this flag affects the total particle multiplicity, when studied as a function of collision centrality. The N_{part}-normalized integrated yield (dN/dy) as a function of N_{part} (centrality) seems to follow a monotonic decrease with an increase of N_{part} for pions, kaons, and protons. However, this seems to be almost independent of centrality for ϕ and Λ. Furthermore, we have checked explicitly that when the decay of ϕ and K_s^0 is allowed the dN/dy for all the identified particles seems to show a monotonic rise with collision centrality.

[1]Initial eccentricity for Xe+Xe, (0–5)% central collisions, $\epsilon_2 \approx 0.24 \pm 0.03$ in random θ and ϕ orientations.

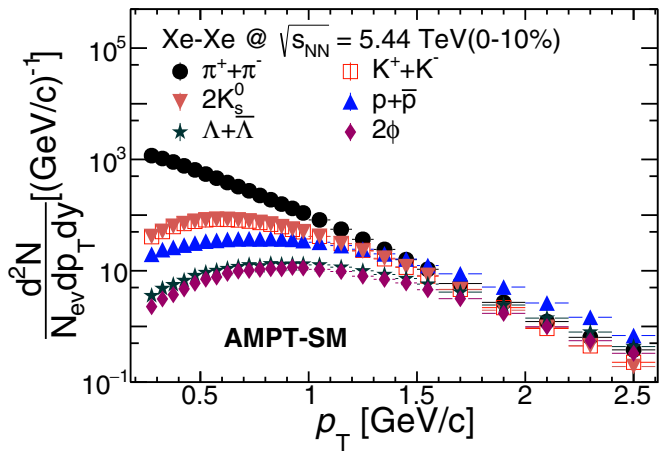

FIG. 2. p_T spectra of identified particles in Xe+Xe collisions at $\sqrt{s_{NN}} = 5.44$ TeV for 0–10% centrality using AMPT-SM. Different symbols show different particle species. The vertical lines in the results show the statistical uncertainties.

III. RESULTS AND DISCUSSIONS

As described in the previous section, we have generated events using the AMPT model in different centralities for Xe+Xe collisions at mid-rapidity for $\sqrt{s_{NN}} = 5.44$ TeV, so that the results could be compared with the corresponding ALICE/CMS experimental data, when they become available. We study the p_T spectra and integrated yield of identified particle production such as $(\pi^+ + \pi^-)$, $(K^+ + K^-)$, K^0_s, $(p + \bar{p})$, ϕ, and $(\Lambda + \bar{\Lambda})$. We also study the p_T-differential and p_T-integrated particle ratios to $(\pi^+ + \pi^-)$ and $(K^+ + K^-)$. From here onwards, $(\pi^+ + \pi^-)$, $(K^+ + K^-)$, $(p + \bar{p})$ and $(\Lambda + \bar{\Lambda})$ are denoted as pions (π), kaons (K), protons (p), and Λ, respectively. As the particle production mechanisms are highly dependent on the transverse momentum range—e.g., when at intermediate p_T, coalescence becomes the major mechanism; at high p_T, the fragmentation takes over—it is worth studying p_T-differential particle ratios. This is the prime focus of the present work.

In Fig. 2, we show p_T spectra of identified hadrons for 0–10% central collisions of Xe+Xe at mid-rapidity ($|\eta| < 0.8$). Different symbols represent the p_T spectra for various particle species. For pions, the lightest hadron, the production is maximum. At low p_T, we observe a mass-dependent behavior of the produced particles. The global mass ordering is violated as the production of ϕ is lesser compared to Λ. This behavior is similar to the experimental data from ALICE at the LHC [46]. While pions show almost an exponentially decreasing behavior, other particles' spectra show a dip at $p_T < 0.5$ GeV/c and they approach the pion spectra at intermediate p_T. This behavior could be due to the radial flow effects in a medium as the radial flow pushes the particles from low p_T to intermediate p_T [47]. Also, these shapes of the p_T spectra may be due to the coalescence mechanism [48] at low and intermediate momenta, and/or the reason might also be the

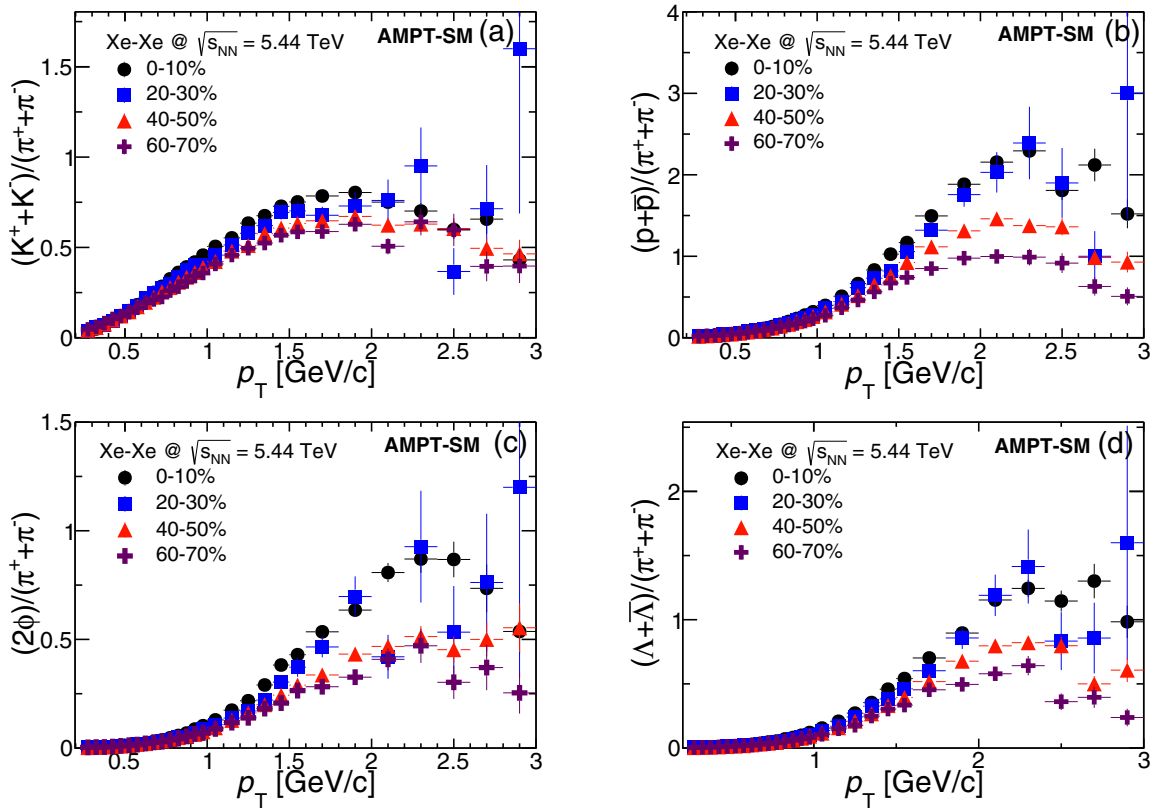

FIG. 3. p_T-differential particle ratios of kaons (a), protons (b), ϕ (c), and Λ (d) to pions in Xe+Xe collisions at $\sqrt{s_{NN}} = 5.44$ TeV. Different symbols show various centrality bins. The vertical lines in the data points are the statistical uncertainties.

production of high-p_T jets [41,49] caused by the fragmentation mechanism, but its effects are mostly found beyond the intermediate momentum region. It would be interesting to study the kinetic freeze-out properties in Xe+Xe collisions. Taking the (0–10)% centrality class and pion p_T spectra, we observe the average radial flow velocity to be $\langle\beta_r\rangle = 0.45 \pm 0.04$ and the $T_{\rm kin} = 109 \pm 12$ MeV. This estimation is done by fitting the Boltzmann-Gibbs blast wave model (BGBW) [50] to the p_T spectra up to $p_T \approx 3$ GeV/c. We have assumed a linear velocity profile in BGBW, which considers the produced fireball as a hard-sphere uniform-density particle source. A centrality dependent study shows that both $T_{\rm kin}$ and $\langle\beta_r\rangle$ are centrality dependent: higher radial flow in central collisions results in a drop in $T_{\rm kin}$, as was earlier observed in heavy-ion collisions [51].

Figure 3 shows p_T-differential particle ratios of kaons, protons, ϕ, and Λ to pions at different centralities. All the particle ratios with respect to π increase as a function of p_T. Considering the K-to-π ratio as a measure of strangeness, we observe enhancement of strangeness production as a function of p_T. This enhancement has a weak dependence on centrality at low p_T, while it strongly depends on centrality in the intermediate-p_T region. At intermediate p_T, the strangeness production is maximum for central collisions and it decreases with centrality. A similar behavior is observed for the case of Λ-to-π ratio, where Λ has the same strangeness content as K. However, the K-to-π ratio rises more rapidly than the ϕ-to-π ratio, which is more gradual. The reason may be due to the higher probability of a strange quark finding an up or a down quark to form kaons rather than finding its antistrange quark to form a ϕ meson in the low momentum region. As we move from low particle momenta to the intermediate momentum region where particle momentum is comparable to or more than the mass of the strange (s) quark, the probability of $s\bar{s}$ production increases considerably so that the ϕ-to-π ratio is found to increase. However, at higher momentum, greater numbers of u and d quarks are also produced compared to s quarks so that both ratios also start to drop beyond $p_T \approx 2$ GeV. Similar trends of particle ratios are also observed in p+Pb and Pb+Pb collisions [52,53].

Figure 3(b) shows the ratio of p to π, which is a ratio between lightest baryons to lightest mesons, which serves as a proxy of baryon-to-meson ratio. We have found that the trend is similar to other ratios but the values are quite different for p-to-π ratios. For most central Xe+Xe collisions, the p-to-π and Λ-to-π ratios are more than 1 in the intermediate-p_T region, which indicates that the baryon production is higher compared to the lightest meson in the intermediate-p_T region. We will revisit this behavior at the end of this section.

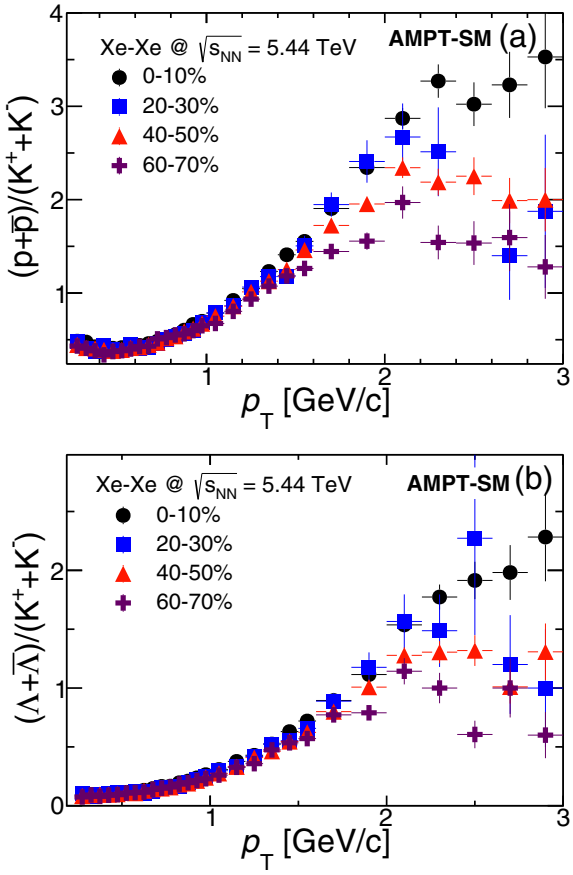

FIG. 4. p_T-differential p-to-K (a) and Λ-to-K (b) ratios for various centrality bins in Xe+Xe collisions at $\sqrt{s_{NN}} = 5.44$ TeV. The vertical lines in the data points are the statistical uncertainties.

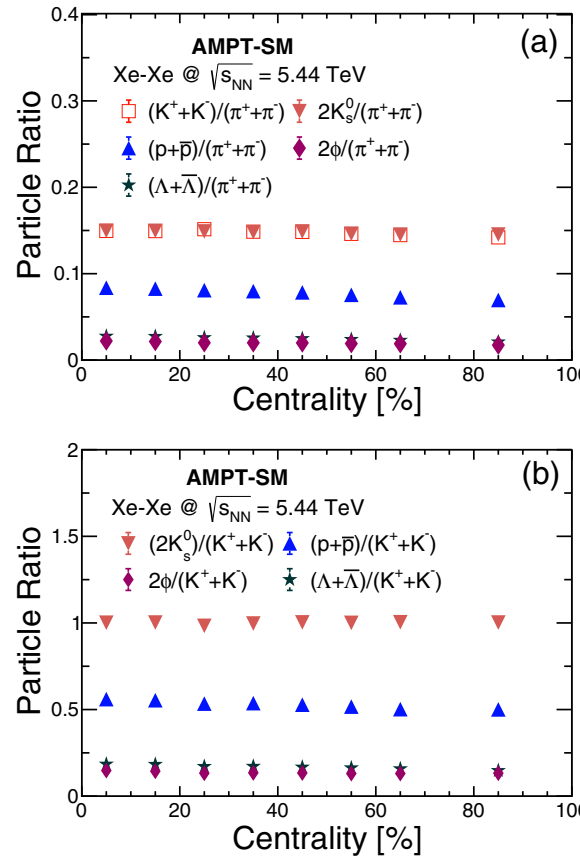

FIG. 5. p_T-integrated ratios of identified particles to pions (a) and kaons (b) as a function of centrality. Different symbols are for different particles. The statistical uncertainties are within symbol sizes.

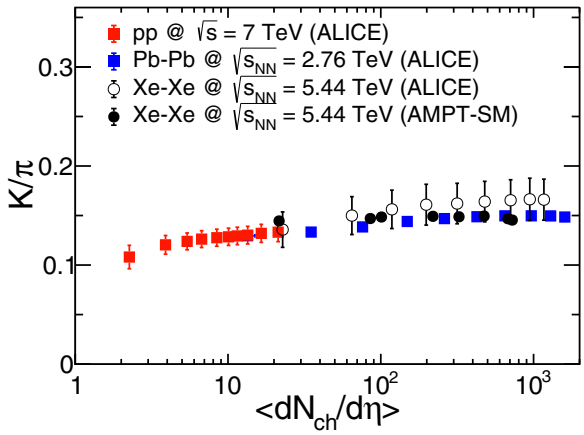

FIG. 6. p_{T}-integrated kaon-to-pion ratio as a function of charged-particle multiplicity for $p+p$ collisions at $\sqrt{s}=7$ TeV, Pb+Pb collisions at $\sqrt{s_{NN}}=2.76$ TeV, and Xe+Xe collisions at $\sqrt{s_{NN}}=5.44$ TeV. The ratios for $p+p$, Xe+Xe, and Pb+Pb collisions are from ALICE experimental data [46,54,57]. The ratio for Xe+Xe collisions from AMPT-SM seems to agree with the experimental data within uncertainties. The experimental data from $p+p$ collisions are for K_s^0/π, while for others the ratio is $(K^+ + K^-)/(\pi^+ + \pi^-)$.

Figure 4 represents the ratios of baryons to lightest strange meson, K. The upper panel of the figure shows p-to-K ratio and the lower panel of the figure shows Λ-to-K ratio as a function of p_{T} for collisions at different centralities. Both the ratios are independent of centrality at low p_{T} while they depend on centrality in the intermediate-p_{T} ranges. For a given p_{T} bin, after $p_{\mathrm{T}} > 1$ GeV/c, the ratios decrease with centrality. This trend is similar to the particle ratios with respect to π in Fig. 3.

Figure 5 shows the p_{T}-integrated ratios of identified hadrons over pions and kaons as a function of centrality. It is very interesting to see that while differential particle ratios show strong dependence with centrality (for $p_{\mathrm{T}} > 1$ GeV/c), the integrated particle ratios show no centrality dependence. This indicates that the relative particle production with respect to pion does not depend on the centrality. This is due to the fact that the integrated yield is dominated by low-p_{T} ($p_{\mathrm{T}} <$ 1 GeV/c) particles. Assuming both centrality and charged-particle multiplicities are used as a proxy for the system size, the centrality-dependent particle ratios of p to π and ϕ to π as a function of centrality in Xe+Xe collisions at $\sqrt{s_{NN}}=5.44$ TeV reproduce qualitatively (within uncertainties) the preliminary results as a function of charged-particle multiplicity of ALICE at the LHC [9,54]. Also, the trends of these ratios are similar to the experimental data in Pb+Pb collisions at $\sqrt{s_{NN}}=2.76$ and 5.02 TeV reported by ALICE [9,46,54–56].

Figure 6 shows the p_{T}-integrated kaon-to-pion ratio as a function of charged-particle multiplicity for $p+p$ collisions at $\sqrt{s}=7$ TeV, Pb+Pb collisions at $\sqrt{s_{NN}}=2.76$ TeV, and Xe+Xe collisions at $\sqrt{s_{NN}}=5.44$ TeV. The ratios for $p+p$ and Pb+Pb collisions are from experimental data [46,57]. The ratio for Xe+Xe collisions are from AMPT-SM and are compared to the ALICE experimental results [54]. We observe that AMPT-SM predictions seem to match with the experimental data within uncertainties. Although data are from different energies and collision systems (viz., Pb+Pb, Xe+Xe, and $p+p$), the proxy of strangeness enhancement, K/π seems to follow a scaling with final state charged particle multiplicity, which in our opinion is a very good observation. On a finer scale, the K-to-π ratio seems to show an increasing

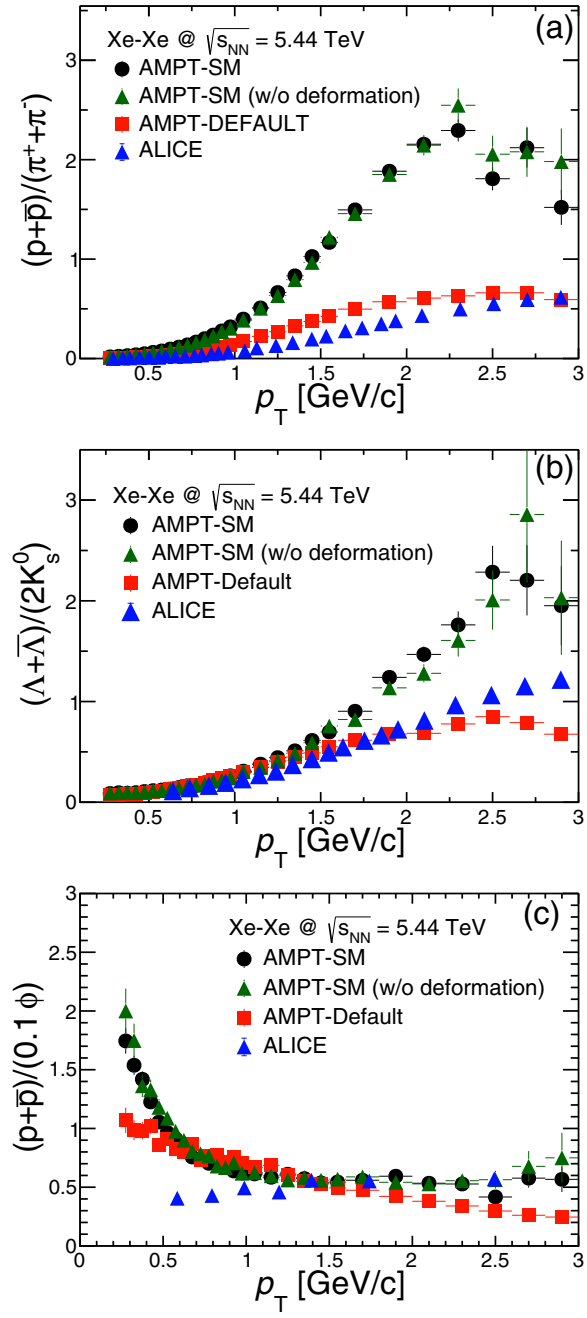

FIG. 7. p_{T}-differential p-to-π (a), Λ-to-K_s^0 (b), and p-to-ϕ (c) ratios for most central (0–10%) Xe+Xe collisions at $\sqrt{s_{NN}}=5.44$ TeV. Red and black markers are predictions from AMPT-Default and AMPT-SM, respectively. The ALICE preliminary data [54] are shown in blue markers. The error bars in the results from models are the statistical uncertainties.

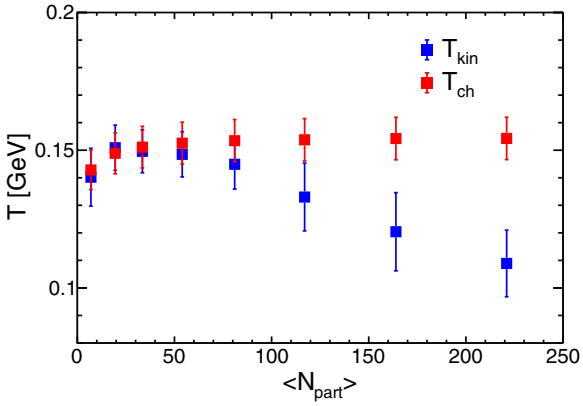

FIG. 8. The kinetic freeze-out temperature $T_{\rm kin}$ and the chemical freeze-out temperature $T_{\rm ch}$ as a function of collision centrality in Xe+Xe collisions at $\sqrt{s_{NN}} = 5.44$ TeV.

trend, which indicates strangeness enhancement with system size. It would be interesting to have experimental data for $p + p$ collisions at $\sqrt{s} = 5.02$ TeV and $p +$ Pb collisions at $\sqrt{s_{\rm NN}} = 5.02$ TeV to have a proper conclusion of this interesting observation.

Figure 7 shows the comparison of $p_{\rm T}$-differential p-to-π, Λ-to-K^0_s, and p-to-ϕ ratios for most central (0–10%) Xe+Xe collisions from AMPT-SM with the AMPT-Default version. Also, they are compared with the preliminary experimental data [54]. For p-to-π and Λ-to-K^0_s ratios, it is observed that the AMPT-Default version is closer to the experimental data than AMPT-SM, especially for $p_T > 1$ GeV/c. It seems that although AMPT-SM describes the elliptic flow of the charged particles of experimental data [58] better than AMPT-Default, in the case of stable particle ratios AMPT-Default does a better job than AMPT-SM. This may be due to the coalescence mechanism involved in AMPT-SM, which affects the particle production at intermediate $p_{\rm T}$. However, in the case of the p-to-ϕ ratio both versions of AMPT fail to explain the experimental data at low $p_{\rm T}$. At intermediate and high $p_{\rm T}$, the AMPT-SM prediction is closer to the experimental data. According to hydrodynamics-inspired models, particles with similar masses should have similar particle spectra at low $p_{\rm T}$. It is found that the ratio is flat for experimental data over all the $p_{\rm T}$ region, whereas for AMPT it decreases up to $p_{\rm T} \approx 1$ GeV/c and then remain flat over the higher $p_{\rm T}$ region.

We have explicitly observed that the particle ratios are independent of nuclear deformation in Xe+Xe collisions. However, it should also be mentioned here that the identified particle $p_{\rm T}$ spectra might be sensitive to nuclear deformation for central Xe+Xe collisions. For the case of deformation, the particle yield ratios are found to be comparable to the case of a spherical Xe nucleus. These findings indicate that nuclear deformation is insensitive to chemical freeze-out in Xe+Xe collisions. Similar results are observed when particle ratios calculated from U+U collisions are compared to Au+Au collision systems [7].

We study chemical freeze-out temperature $T_{\rm ch}$ as a function of collision centrality measured through $\langle N_{\rm part}\rangle$ in Xe+Xe collisions at $\sqrt{s_{NN}} = 5.44$ TeV using AMPT. This is shown in Fig. 8 along with a comparison of kinetic freeze-out temperature $T_{\rm kin}$. The $T_{\rm ch}$ for (0–10)% centrality is found to be around 154 ± 8 MeV, which is comparable with $p +$ Pb collisions at $\sqrt{s_{NN}} = 5.02$ TeV [59]. As expected, the present analysis of particle ratios reveals $T_{\rm ch}$ to be independent of collision centrality in Xe+Xe collisions. Here we have taken the discussed particle ratios and have assumed a grand canonical ensemble in the thermal model [60] taking $\mu_B = 0$ and keeping $T_{\rm ch}$, the strangeness saturation factor γ_s, and the fireball radius as the free parameters. The kinetic freeze-out temperature is found to be highly dependent on collision centrality.

IV. SUMMARY

We have studied the $p_{\rm T}$ spectra, integrated yield, and particle ratios of identified particles for Xe+Xe collisions at $\sqrt{s_{NN}} = 5.44$ TeV using AMPT. Our findings are the following:

(1) We have reported the simulation studies of identified particle production in Xe+Xe collisions at $\sqrt{s_{NN}} = 5.44$ TeV using the AMPT model. This can be compared with experimental data, when they become available. In particular, the effect of nuclear deformation warrants a simulation study, which, through this work, would result in better understanding of experimental findings.

(2) A BGBW analysis of pion $p_{\rm T}$ spectra up to $p_{\rm T} \approx 3$ GeV/c for (0–10)% centrality class shows the radial flow velocity $\langle\beta_r\rangle = 0.45 \pm 0.04$ and the kinetic freeze-out temperature $T_{\rm kin} = 109 \pm 12$ MeV. As observed earlier in heavy-ion collisions at RHIC, the radial flow velocity decreases and the the kinetic freeze-out temperature increases towards peripheral collisions.

(3) We observe enhancement of strangeness production as a function of $p_{\rm T}$. This enhancement has a weak dependence on centrality at low $p_{\rm T}$, while it strongly depends on centrality in the intermediate-$p_{\rm T}$ region.

(4) We observe that the differential particle ratios show strong dependence with centrality (for $p_{\rm T} > 1$ GeV/c) while the integrated particle ratios show no centrality dependence.

(5) It is indeed interesting to note that the proxy of strangeness enhancement, the K/π ratio, when studied as a function of final state charged particle multiplicity for $p + p$, Xe+Xe, and Pb+Pb collisions at different collision energies at the LHC, shows a scaling behavior indicating that the final state multiplicity drives the particle production. The availability of future experimental data at other different energies for $p + p$, $p +$ Pb, and Pb+Pb collisions at the LHC would help improve understanding of this observation.

(6) We have found that for p-to-π and Λ-to-K^0_s ratios, the AMPT-Default version is closer to the experimental data than AMPT-SM, especially for $p_T > 1$ GeV/c. This may be due to the coalescence mechanism

involved in AMPT-SM, which affects the particle production at intermediate p_T.

(7) For the p-to-ϕ ratio, the AMPT-SM version does a better job compared to the AMPT-Default version. The AMPT-SM version seems to reproduce the experimental data after $p_T \approx 1$ GeV/c, which is expected by the hydrodynamics-inspired models.

(8) It is explicitly observed from these extensive studies that the particle ratios are insensitive to nuclear deformation, at least in the case of Xe+Xe collisions. However, it should also be noted here that the particle spectra are sensitive to nuclear deformation.

(9) Thermal model analysis of the particle ratios in Xe+Xe collisions at $\sqrt{s_{NN}} = 5.44$ TeV using AMPT gives the chemical freeze-out temperature for (0–10%) centrality, $T_{\rm ch} = 154 \pm 8$ MeV. Further, we have found $T_{\rm ch}$ to be independent of collision centrality, whereas the $T_{\rm kin}$ is highly centrality dependent. This is in line with the earlier findings at the RHIC [51] and LHC [59].

We believe the present exhaustive study of the particle spectra, ratios, and freeze-out criteria would be quite helpful in understanding the Xe+Xe collisions at LHC energies with nuclear deformation, when the corresponding experimental data become available.

ACKNOWLEDGMENTS

The authors acknowledge the financial support from the ALICE Project No. SR/MF/PS-01/2014-IITI(G) of the Department of Science & Technology, Government of India. R.R. and S.T. acknowledge the financial support by the DST-INSPIRE program of the Government of India. The authors would like to acknowledge the usage of resources of the LHC grid computing facility at VECC, Kolkata. Dr. Swatantra K. Tiwari is acknowledged for initial discussions and Dr. Zi-Wei Lin for the necessary permission for implementing the nuclear deformation in AMPT. The authors are thankful to Arvind Khuntia for his help in the thermal model analysis.

[1] S. A. Bass, M. Gyulassy, H. Stoecker, and W. Greiner, J. Phys. G **25**, R1 (1999).
[2] S. Voloshin and Y. Zhang, Z. Phys. C **70**, 665 (1996).
[3] J. Adams *et al.* (STAR Collaboration), Phys. Rev. Lett. **92**, 052302 (2004).
[4] L. Adamczyk *et al.* (STAR Collaboration), Phys. Rev. Lett. **115**, 222301 (2015).
[5] C. Nepali, G. Fai, and D. Keane, Phys. Rev. C **73**, 034911 (2006).
[6] Md. R. Haque, Z.-W. Lin, and B. Mohanty, Phys. Rev. C **85**, 034905 (2012).
[7] S. K. Tripathy, M. Younus, Z. Naik, and P. K. Sahu, Nucl. Phys. A **980**, 81 (2018)
[8] G. Giacalone, J. Noronha-Hostler, M. Luzum, and J. Y. Ollitrault, Phys. Rev. C **97**, 034904 (2018).
[9] S. Tripathy (ALICE Collaboration), Nucl. Phys. A **982**, 180 (2019).
[10] B. I. Abelev *et al.* (STAR Collaboration), Phys. Rev. C **75**, 054906 (2007).
[11] A. Adare *et al.* (PHENIX Collaboration), Phys. Rev. Lett. **98**, 162301 (2007).
[12] A. Adare *et al.* (PHENIX Collaboration), Phys. Rev. C **85**, 064914 (2012).
[13] S. Singha and Md. Nasim, Phys. Rev. C **93**, 034908 (2016).
[14] Liang Zheng *et al.*, Eur. Phys. J. A **53**, 124 (2017).
[15] B. Kim (ALICE Collaboration), Nuc. Phys. A **982**, 279 (2019).
[16] S. Acharya *et al.* (ALICE Collaboration), Phys. Lett. B **784**, 82 (2018).
[17] B. B. Abelev *et al.* (ALICE Collaboration), Phys. Rev. C **91**, 024609 (2015)
[18] Z. w. Lin and C. M. Ko, Phys. Rev. C **65**, 034904 (2002).
[19] L. W. Chen, V. Greco, C. M. Ko, and P. F. Kolb, Phys. Lett. B **605**, 95 (2005).
[20] B. I. Abelev *et al.* (STAR Collaboration), Phys. Rev. Lett. **99**, 112301 (2007).
[21] Z. W. Lin, C. M. Ko, B. A. Li, B. Zhang, and S. Pal, Phys. Rev. C **72**, 064901 (2005).
[22] X. N. Wang and M. Gyulassy, Phys. Rev. D **44**, 3501 (1991).
[23] C. Loizides, J. Kamin, and D. d'Enterria, Phys. Rev. C **97**, 054910 (2018).
[24] H. Masui, B. Mohanty, and N. Xu, Phys. Letts. B **679**, 440 (2009).
[25] P. Dasgupta, R. Chatterjee, and D. K. Srivastava, Phys. Rev. C **95**, 064907 (2017).
[26] O. S. K. Chaturvedi *et al.*, Eur. Phys. J. Plus **132**, 430 (2017).
[27] A. Singh *et al.*, Eur. Phys. J. C **78**, 419 (2018).
[28] R. Hofstadter, Nobel Lecture, December 11, 1961.
[29] R. D. Woods and D. S. Saxon, Phys. Rev. **95**, 577 (1954).
[30] D. L. Hendrie, N. K. Glendenning, B. G. Harvey, O. N. Jarvis, H. H. Duhm, J. Saudinos, and J. Mahoney, Phys. Lett. B **26**, 127 (1968).
[31] P. Moller, J. R. Nix, W. D. Myers, and W. J. Swiatecki, At. Data Nucl. Data Tables **59**, 185 (1995).
[32] D. A. Varshalovich, A. N. Moskalev, and V. K. Khersonskii, *Quantum Theory of Angular Momentum* (World Scientific, Singapore, 1988), Chap. 5.
[33] C. E. Flores, Ph.D. thesis, University of California, Davis, 2017, http://nuclear.ucdavis.edu/thesis/CEF_Thesis_Final.pdf.
[34] Schenke *et al.*, Phys. Rev. C **89**, 064908 (2014).
[35] C. Nepali, G. Fai, and D. Keane, Phys. Rev. C **76**, 051902(R) (2007).
[36] S. Pal and M. Bleicher, Phys. Lett. B **709**, 82 (2012).
[37] B. Zhang, Comput. Phys. Commun. **109**, 93 (1998).
[38] V. Greco, C. M. Ko, and P. Levai, Phys. Rev. Lett. **90**, 202302 (2003).
[39] B. Li, A. T. Sustich, B. Zhang, and C. M. Ko, Int. J. Mod. Phys. E **10**, 267 (2001).
[40] B. A. Li and C. M. Ko, Phys. Rev. C **52**, 2037 (1995).
[41] V. Greco, C. M. Ko, and P. Levai, Phys. Rev. C **68**, 034904 (2003).

[42] R. J. Fries, B. Muller, C. Nonaka, and S. A. Bass, Phys. Rev. Lett. **90**, 202303 (2003).
[43] R. J. Fries, B. Muller, C. Nonaka, and S. A. Bass, Phys. Rev. C **68**, 044902 (2003).
[44] Z. Feng, G. M. Huang, and F. Liu, Chin. Phys. C **41**, 024001 (2017).
[45] S. Tripathy, S. De, M. Younus, and R. Sahoo, Phys. Rev. C **98**, 064904 (2018).
[46] B. Abelev *et al.* (ALICE Collaboration), Phys. Rev. C **88**, 044910 (2013).
[47] S. Tripathy, S. K. Tiwari, M. Younus, and R. Sahoo, Eur. Phys. J. A **54**, 38 (2018).
[48] L. Zhu, H. Zheng, and R. Kong, arXiv:1811.09510.
[49] M. Younus, S. Tripathy, S. K. Tiwari, and R. Sahoo, arXiv:1803.01578.
[50] E. Schnedermann, J. Sollfrank, and U. Heinz, Phys. Rev. C **48**, 2462 (1993).
[51] B. I. Abelev *et al.* (STAR Collaboration), Phys. Rev. C **79**, 034909 (2009).
[52] J. Adam (ALICE Collaboration), Eur. Phys. J. C **75**, 226 (2015).
[53] B. Abelev (ALICE Collaboration), Phys. Lett. B **728**, 25 (2014).
[54] F. Bellini (ALICE Collaboration), Nucl. Phys. A **982**, 427 (2019).
[55] B. B. Abelev *et al.* (ALICE Collaboration), Phys. Lett. B **736**, 196 (2014).
[56] A. K. Dash (ALICE Collaboration), Nucl. Phys. A **982**, 467 (2019).
[57] J. Adam *et al.* (ALICE Collaboration), Nat. Phys. **13**, 535 (2017).
[58] Z. W. Lin, Acta Phys. Pol. Supp. **7**, 191 (2014).
[59] N. Sharma, J. Cleymans, B. Hippolyte, and M. Paradza, Phys. Rev. C **99**, 044914 (2019).
[60] S. Wheaton, J. Cleymans, and M. Hauer, arXiv:1108.4588.